Chemical Science

ROYAL SOCIETY OF CHEMISTRY

EDGE ARTICLE

View Article Online
View Journal | View Issue

Cite this: *Chem. Sci.*, 2022, **13**, 7541

All publication charges for this article have been paid for by the Royal Society of Chemistry

High-performance potassium poly(heptazine imide) films for photoelectrochemical water splitting†

Xiaochun Li, Xiaoxiao Chen, Yuanxing Fang, * Wei Lin, Yidong Hou, Masakazu Anpo, Xianzhi Fu and Xinchen Wang *

Received 10th April 2022
Accepted 31st May 2022

DOI: 10.1039/d2sc02043b

rsc.li/chemical-science

Photoelectrochemical (PEC) water splitting is an appealing approach by which to convert solar energy into hydrogen fuel. Polymeric semiconductors have recently attracted intense interest of many scientists for PEC water splitting. The crystallinity of polymer films is regarded as the main factor that determines the conversion efficiency. Herein, potassium poly(heptazine) imide (K-PHI) films with improved crystallinity were *in situ* prepared on a conductive substrate as a photoanode for solar-driven water splitting. A remarkable photocurrent density of *ca.* 0.80 mA cm^{-2} was achieved under air mass 1.5 global illumination without the use of any sacrificial agent, a performance that is *ca.* 20 times higher than that of the photoanode in an amorphous state, and higher than those of other related polymeric photoanodes. The boosted performance can be attributed to improved charge transfer, which has been investigated using steady state and *operando* approaches. This work elucidates the pivotal importance of the crystallinity of conjugated polymer semiconductors for PEC water splitting and other advanced photocatalytic applications.

Introduction

Solar-driven water splitting for hydrogen fuel production using a photoelectrochemical (PEC) platform is an appealing strategy by which to sustain energy demand.[1–4] In the PEC system, semiconducting photoelectrodes with the properties of the efficient absorption of visible light and high quantum yield have been researched for almost half a century,[5] and a variety of materials, including metal oxides,[6–9] metal oxynitrides,[10,11] perovskites,[12] polymers,[13] metal–organic frameworks[14–16] and other materials,[17–21] have been reported. Among them, conjugated polymers have received broad attention recently.[22] Their advantages, namely chemical sustainability and cost-effectiveness, have offered new opportunities for practical applications.[23] In addition, the thermodynamics of the semiconducting polymers can be optimized by versatile organic chemistry protocols.[24–27]

The crystallinity of semiconducting polymers has been recognized as being the main factor that influences the photocatalytic performance,[28] since the crystallinity has been thought to be highly associated with the transfer of charge carriers and their recombination in photocatalysts.[29] However, as a macromolecular species with multiple repeating units, polymers are difficult to crystallize.[30] Typically, the polymer structure should be regularly arranged with a minimum number of pendant groups for intimate packing of the units.[31] In addition, chemical bonding is preferable to form units with strong intermolecular forces. As an example, amorphous polymeric carbon nitride (PCN), namely melon, can be crystalized *via* an ionothermal synthesis method to form poly(triazine imide) (PTI)[32,33] or poly(heptazine imide) (PHI).[34,35] In this process, the molten salt has been known to drive the interunit arrangement by increasing the intermolecular forces. In addition, the free ions from molten salts are available to intercalate into the polymer texture, leading to the strengthening of the frameworks of polymer crystals. An apparent quantum efficiency of *ca.* 60% has been realized at 420 nm excitation for photocatalytic hydrogen evolution by a PHI photocatalyst.[36] Moreover, PTI single crystals were recently reported to achieve an apparent quantum efficiency of up to 12% for photocatalytic overall water splitting at an illumination wavelength of 365 nm.[37] These efficiencies are two orders of magnitude higher than that of the amorphous melon-based photocatalyst.

The migration of photogenerated charge carriers, namely electrons and holes, is of particular importance for photoelectrodes since the electrons or holes must travel through the entirety of photocatalytic films to the surfaces to participate in redox reactions.[38–40] In addition, the photocatalytic films are preferable to be anchored on a substrate *via* chemical bonding, allowing the photogenerated charge carriers to transfer from

State Key Laboratory of Photocatalysis on Energy and Environment, College of Chemistry, Fuzhou University, Fuzhou 350116, P. R. China. E-mail: yxfang@fzu.edu.cn; xcwang@fzu.edu.cn

† Electronic supplementary information (ESI) available. See https://doi.org/10.1039/d2sc02043b

the working electrode to the counter electrode for redox reactions.[41,42] *In situ* approaches have been widely studied for inorganic semiconducting materials to allow efficient transfer of the photoexcitation charges.[43] Recent demonstrations have presented the approach to the *in situ* synthesis of melon-based films anchored on a conductive substrate as photoanodes.[44,45] However, it remains a challenge to synthesize PCN films that exhibit crystallinity.[46] Thus, a synthesis method that meets all the requirements, including chemical anchoring between conductive layers and the PCN films, thermodynamics for sufficient polymerization, and intercalation of the supporting ions to strengthen the framework of polymer crystals, still needs to be developed.[47] Nevertheless, there is a strong desire to develop polymeric photoelectrodes with high crystallinity for PEC water splitting to surpass inorganic semiconducting materials in terms of photocurrent density and open up a new avenue for practical applications.[48]

Herein, as a proof-of-concept advance, potassium poly(-heptazine) imide (K-PHI) based photoanodes have been developed for PEC water splitting. The K-PHI films are synthesized by *in situ* polymerization, and they are intimately anchored on a conductive fluorine-doped tin oxide (FTO) substrate by chemical bonding. A remarkable photocurrent density of *ca.* 0.8 mA cm^{-2} has been recorded by illumination of air mass 1.5 global (AM 1.5G) in 1.0 M NaOH electrolyte solution without the use of any sacrificial agents, a much higher performance than those of other related polymeric photoanodes. The improved performance can be attributed to the high crystallinity of the K-PHI films. The manner of the photogenerated charge carrier transfer was investigated using steady state and *operando* approaches, and the importance of crystallization of polymer semiconductors is elucidated for their use in PEC applications.

Experimental

Melamine (10 g) was loaded in a crucible and heated at 400 °C for 1 h at a ramping rate of 2.3 °C min^{-1} in a muffle furnace in air for pre-polymerization. The as-prepared powder (2.0 g) was blended with potassium thiocyanate (KSCN, 1.4 g) as a precursor. FTO glass was cleaned by sequential sonication in acetone, ethanol and deionized water for 10 min, and dried under a nitrogen flow. The precursor was transferred into a crucible, and clean FTO glass was embedded in the as-prepared precursor. The crucible was heated at 500 °C for 4 h at a ramping rate of 2.3 °C min^{-1} in a tubular furnace under the protection of nitrogen, flowing at a rate of 100 cm^3 min^{-1}. Upon cooling to ambient temperature, potassium poly(heptazine) imide (K-PHI) films were formed on FTO glass as a photoanode. Prior to the conducting of PEC water splitting tests, the photoanode was rinsed with deionized water, and sonicated for 10 min to remove the unreacted salt and the unstable aggregates from the surface of the K-PHI films. The photoanode was denoted as K-PHI. As a reference, a melon-based photoanode with low crystallinity was synthesized from a mixed precursor of M400 (2.0 g) and ammonium thiocyanate (NH_4SCN, 1.4 g), and all the other synthesis procedures were the same as that of the preparation of the K-PHI photoanode.

The reference powder-based photoanodes were prepared on the clean FTO glass by drop-coating. Specifically, 95 mg of K-PHI and 5 mg of SnS_2 powder were suspended in 5 mL of deionized water by sonication, at a concentration equivalent to 2.65 at% of SnS_2 in K-PHI. The powdered mixture was collected by filtration and dried at 60 °C under vacuum. The as-prepared powdered sample was denoted as 2.65 at% SnS_2/K-PHI. 5 mg of the powder was dispersed in 800 μL of *N*,*N*-dimethylformamide (DMF) by sonication to form a suspension. The suspension was coated on the pretreated FTO glass and dried under ambient conditions. The dried photoanodes were thermally treated at 300 °C for 1 h. Photoanodes were collected by cooling to room temperature spontaneously.

Scanning electron microscope (SEM, JSM-6700F) images were acquired to investigate the morphology and structure of the melon and K-PHI films. Transmission electron microscopy (TEM, FEI Talos) accompanied by energy dispersive spectroscopy (EDS) was performed to study the chemical structure and crystallinity of the melon and K-PHI films. The samples were prepared by scraping the films from the photoelectrode and dispersing them in ethanol by sonication for 30 min. A copper mesh was used to collect the dispersed powder, which was then dried in an oven at 80 °C for 2 h.

Powder X-ray diffractometry (PXRD) measurements were carried out using a Miniflex 600 diffractometer equipped with a Cu Kα1 radiation source (k = 1.5406 Å) to study the crystallinity of the samples. Fourier-transform infrared (FTIR) spectra were recorded by a Nicolet 670 FTIR spectrometer with KBr as the diluent. Raman spectra were recorded by a HORIBA LabRAM HR Evolution spectroscopy system. X-ray photoelectron spectroscopy (XPS) measurements were recorded by a Thermo ESCALAB 250 instrument with a monochromatized Al Kα line source (200 W) and the peaks were calibrated to the C 1s peak at 284.8 eV. The depth profiles of XPS were measured by a 4 keV Ar^+ ion gun for sputtering the films, and the signals of the different layers of the films were collected after a certain duration of sputtering.

Ultraviolet-visible diffusion reflector spectroscopy (UV-Vis DRS) was conducted using a Varian Cary 500 Scan UV-visible system to study the optical properties of the samples. Room-temperature photoluminescence (PL) spectroscopy and transient decay PL spectra were recorded using a HORIBA Fluorolog-3 spectrophotometer to study the photoexcitation and lifetime at steady state. The excitation wavelength for the emission spectrum was 360 nm. The average lifetimes for the transient decay of the PL spectra were calculated according to the following equation:[49]

$$D_t = \tau_1 I_1 + \tau_2 I_2 + \tau_3 I_3 \quad (1)$$

where τ_i is the lifetime and I_i is the relative intensity.

PEC measurements were recorded on a BioLogic VSP-300 electrochemical system using a three-electrode system. The as-prepared photoanodes were used as the working photoanode and Pt foil (1.0 cm × 1.0 cm) and Ag/AgCl were used as counter and reference electrodes, respectively. The electrolyte solution was 1.0 M NaOH solution (pH *ca.* 14.0). An air mass 1.5 global

(AM 1.5G) solar simulator (Newport, USA) was used as a light source. Linear sweep voltammetry (LSV) and chronoamperometry (CA) measurements were performed with an illumination area of 1.0 cm × 0.5 cm at a scan rate of 50 mV s^{-1}. Nyquist plots and Mott–Schottky measurements were obtained using an electronic impedance spectroscopy (EIS) system in 0.2 M Na_2SO_4 solution (pH value ~6.0). Carrier density was estimated through the Mott–Schottky relation.[50] Incident light-to-electron conversion efficiency (IPCE) was conducted using a xenon lamp (300 W) fitted with a monochromator (Newport, USA) at an illumination of a certain wavelength.[51] The applied bias photon-to-current efficiency (ABPE) was calculated from current–potential curves under AM 1.5G illumination.[52]

The amounts of the evolved gases from the PEC system were analyzed and quantified by a gas chromatograph equipped with a thermal conductive detector (TCD) and a 5 Å molecular sieve column using argon as the carrier gas. Intensity modulated photocurrent spectroscopy (IMPS) measurements were performed on an electrochemical workstation CIMPS system (Zennium Zahner PP211, Germany) with a tungsten lamp in a three-electrode system. IMPS was applied to *in situ* study the dynamics of photoexcitation charge carriers during the oxygen evolution reaction.

Density functional theory (DFT) calculations were carried out *via* the Vienna *ab initio* simulation package (VASP), version 5.4.[53,54] Projector augmented wave (PAW) potentials[55,56] were used to describe the electron–ion interactions and the generalized gradient approximation (GGA) of the Perdew–Burke–Ernzerhof (PBE) functional was used to describe the exchange and correlation interactions.[57] The van der Waals corrections were considered *via* Grimme's D3 method.[58] The wavefunction was expanded using plane waves with a cutoff energy of 450 eV. The Brillouin zone of 2 × 2 × 1 unit cells was sampled using a 1 × 1 × 1 Monkhorst–Pack mesh for structural relaxation of the *k* points, while a denser *k*-point mesh of 2 × 2 × 1 was used for electronic property evaluations.[59] The systems were fully relaxed until the conventional energy was lower than 10^{-4} eV and the Hellmann–Feynman forces were lower than 0.02 eV $Å^{-1}$.

Results and discussion

The synthesis of the K-PHI films generally involved three steps (Fig. S1†). Melamine was used as a precursor, and it was thermally treated for pre-polymerization to partially form a heptazine structure. The as-prepared powder was blended with KSCN as the precursors to grow K-PHI films on FTO glass. Details of the polymerization are illustrated in Fig. 1a. KSCN is molten, leading to the formation of a SnS_2 layer on top of the FTO glass initially. Thus, the formed SnS_2 layer acts as crystal seeds for the subsequent growth of the K-PHI films. The molten KSCN works to increase the intermolecular force of heptazine, promoting the polymerization of PCN. The K^+ ions from KSCN are enabled to insert into the polymeric framework to from a rigid PHI structure.

The K-PHI films were studied by SEM. As shown in Fig. 1b, a homogeneous morphology is observed. The mean thickness of the K-PHI films are *ca.* 3.0 μm, as revealed by the cross-sectional image shown in Fig. 1c. In comparison with the melon films (Fig. S2†), the K-PHI is distinguishable from the rigid fraction. The thickness of the melon films were observed to be relatively larger than that of K-PHI (Fig. S3†). These observations are probably owing to the polymerization of K-PHI being highly related to the SnS_2 crystal seeds, which are available only near to the surface of the FTO glass.

The morphology of K-PHI was further studied by TEM. Two characteristic crystal facets of K-PHI are shown in Fig. 1e and f, namely, the $[\bar{1}10]$ and [002] planes with distances of the lattice fringes of 1.01 nm and 0.32 nm, respectively. A schematic illustration of the K-PHI along the $[\bar{1}10]$ and [002] directions is presented in Fig. 1d. In comparison to K-PHI, it was difficult to probe the crystallinity of the amorphous melon films (Fig. S4†). Moreover, selected area electron diffraction (SAED) patterns further confirmed the improved crystallinity of K-PHI (Fig. S5†). Note that the crystal facet of SnS_2 was detected among those of K-PHI (Fig. S6†). This formation is significant as it is considered to be due a reaction prior to the K-PHI polymerization, thus meaning that S is available to bind the heptazine group. The surface structure of the K-PHI was investigated by scanning TEM (STEM) accompanied by EDS. The image observed using the high-angle annular dark field (HAADF) technique is shown in Fig. 1g. Corresponding to this image, the elements C, K, and N can be observed in Fig. 1h, i and j, respectively, which confirm the formation of the K-PHI crystal structure. Sn and S were also detected (Fig. S7†). Since SnS_2 is also a type of photocatalyst, it is thought that SnS_2 affects the performance of PEC water splitting.[60] Therefore, in order to check this effect, the ratio of elements was defined by EDS (Fig. S8†). The atomic fractions of S and Sn were *ca.* 1.79 at% and 0.86 at%, respectively. The major composition was C and N, with an atomic percentage of 90.04%. The ratio of C and N was close to 3 : 4, and the ratio of K to N was 1 : 32. These results are in good agreement with the molecular structure of K-PHI, and a small fraction of SnS_2 was found to be present between the K-PHI films and FTO glass, at 2.65 at%.

The crystal phases of the photoanodes were studied by PXRD (Fig. S9†). The observed main peaks can be attributed to the FTO substrate (JCPDS No. 46-1088). Therefore, in order to avoid the effect of the FTO substrate, the moieties of K-PHI films were peeled off from the FTO substrate and then studied, as shown in Fig. 2a. In the case of melon, the characteristic peaks at 13.0° and 27.5° can be assigned to the amorphous structure of PCN.[61] However, in the case of K-PHI, the dominant peak at 28.1° can be ascribed to the [002] plane of K-PHI and is related to the π–π stacking of the heptazine subunits, which is much sharper than that of melon due to the phase transition with improved crystallinity of K-PHI.[62] It is worth noting the fact that this diffraction angle is slightly higher than that of melon owing to the decreased interlayer distance, which can be attributed to the enhanced interaction among the layers. In addition, the minor peak at 8.1° can be ascribed to the $[\bar{1}10]$ plane, corresponding to increased in-plane periodicity. The minor peaks at 32.3°, 35.4° and 43.2° can be attributed to the (001) reflections, owing to the intercalation of metal ions in K-PHI as a result of its ionothermal synthesis.[63] The peaks at 15.0° and 32.1° can be

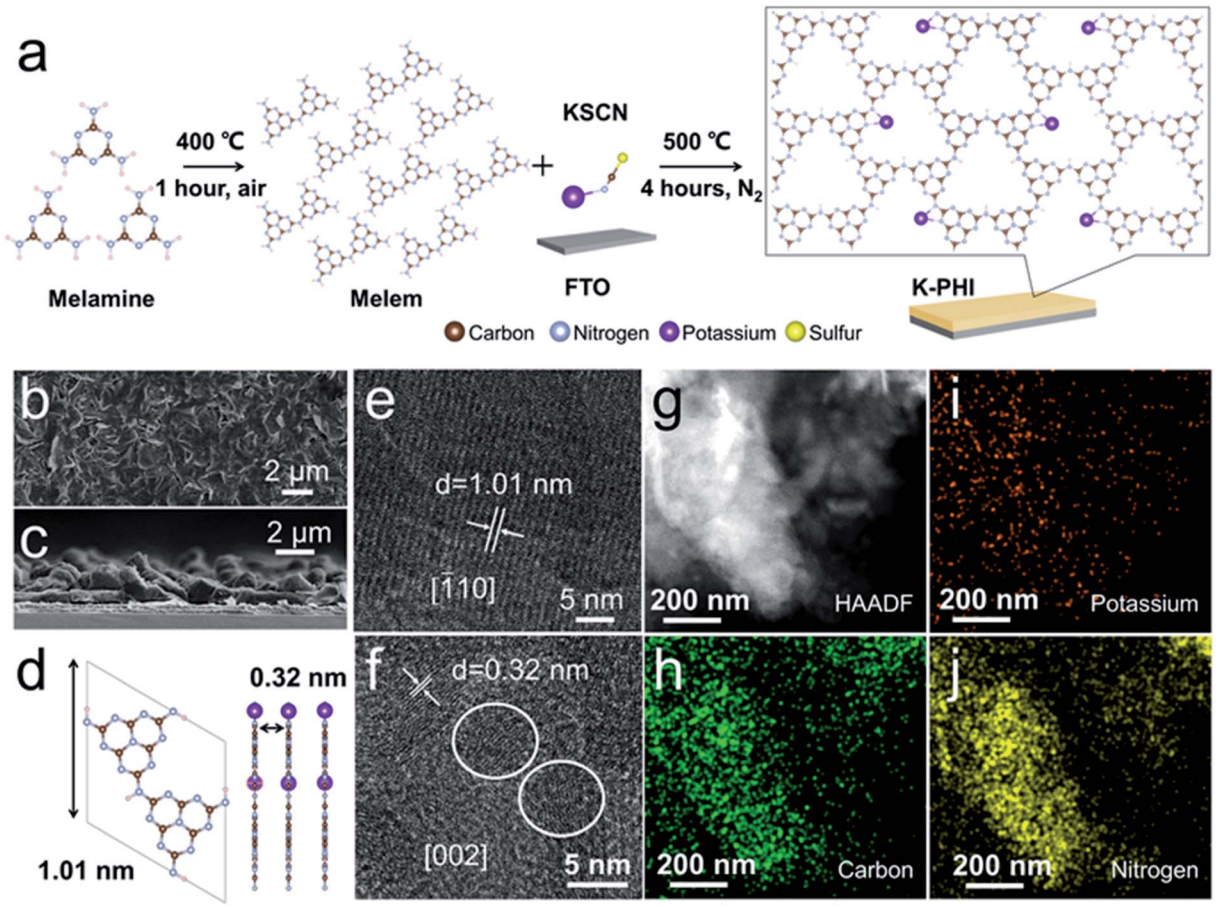

Fig. 1 (a) Illustration of the polymerization of K-PHI films on an FTO substrate. (b) Top view and (c) cross-sectional view of the K-PHI photoanode. TEM images of K-PHI from the (e) [$\bar{1}$10] and (f) [002] planes with the corresponding schematic illustrations shown in (d). (g) TEM images of K-PHI recorded using HAADF techniques with EDS studies on (h) C, (i) K, and (j) N.

attributed to the [001] and [101] planes of SnS_2 (JCPDS No. 22-0951), respectively. As shown in Fig. 2b, these results are in good agreement with those of the powder samples prepared using the same approach as that of the photoanodes.

As shown in Fig. 2c, Fourier-transform infrared (FTIR) spectroscopy was conducted to study the chemical structure of the photoanode. Typically, a sharp peak was observed at 810 cm^{-1} that could be attributed to the bending mode of the heptazine ring. Dominant peaks can be observed at around 1200 cm^{-1} to 1700 cm^{-1}, assigned to the stretching modes of the heptazine ring, with these peaks observed for both melon and the K-PHI photoanode. An obvious peak located at 2177 cm^{-1} can be observed in the spectrum of K-PHI, which is attributed to the stretching vibration of the terminal cyano groups. As shown in the Raman spectrum of K-PHI in Fig. 2d, the cyano group is also detected at 2180 cm^{-1}. The presence of the cyano groups in K-PHI is associated with the presence of defects in the heptazine units, with such defects being normally formed during the molten salt synthesis. During polymerization, the molten salt compensates for the thermodynamic difficulty in evolving ammonia, improving the condensation, which results in strengthening the internal forces that promote crystallization. For melon, the Raman spectrum presents dominant peaks at *ca.* 1100 to 1800 cm^{-1}, assigned to the stretching vibrations of C–N. The peaks at 705 cm^{-1} and 765 cm^{-1} can be attributed to the in-plane bending vibrations of C–N=C, and the peak at 978 cm^{-1} is due to the breathing of the symmetric N in the heptazine units. These peaks can also be observed in the Raman spectrum of K-PHI, indicating that both melon and K-PHI are based on heptazine units. An extra peak at 315 cm^{-1} can be observed for K-PHI, attributed to the unique A_{1g} mode of SnS_2 in the K-PHI photoanode.

XPS data were further acquired to study the crystal structure of the K-PHI films. High-resolution C 1s spectra are shown in Fig. 3a, in which two dominant peaks observed at 284.8 eV and 288.1 eV in the C 1s spectra can be assigned to adventitious carbon and sp^2-hybridized carbon (N–C=N) in the heptazine ring, respectively. In addition, a minor peak at 286.3 eV can be attributed to cyano groups, and the peak intensity of this peak for K-PHI is at a higher binding energy than that of melon, in good agreement with the FTIR spectroscopy results. These signals are observed for both the K-PHI and melon photoanodes. K 2p is shown in Fig. 3a, and the two peaks at 295.6 eV and 292.8 eV can be attributed to K $2p_{1/2}$ and K $2p_{3/2}$, respectively. The observation of these peaks clearly indicates that K^+ ions are involved in the K-PHI polymer films. In addition, the

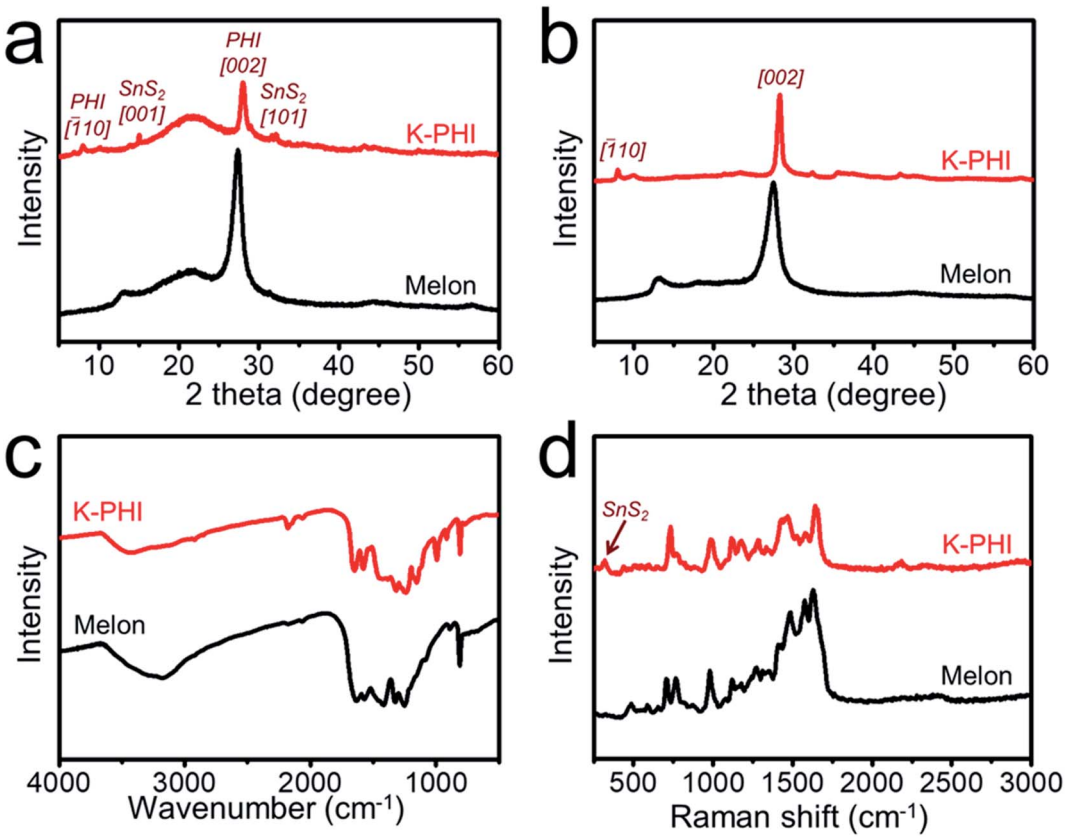

Fig. 2 (a) PXRD patterns of powder samples scraped from films of melon and K-PHI. (b) PXRD patterns of powder samples of melon and K-PHI prepared using the same approaches as for the photoanodes. (c) FTIR spectra of powder samples scraped from the melon and K-PHI films. (d) Raman spectra of the melon and K-PHI photoanodes.

depth profiles of the C 1s and K 2p spectra observed after etching by Ar^+ ion bombardment are shown in Fig. 3a. The C 1s peaks of K-PHI gradually weakened in intensity. This observation can be attributed to the instability of the heptazine ring against Ar^+ ion bombardment. In contrast, the intensity of the K 2p peaks was found to be excellently preserved, indicating the homogeneous presence of K from top to bottom of the K-PHI films. As shown in Fig. 3b, the N 1s peak of K-PHI can be deconvoluted into three peaks with binding energies of 398.6 eV, 399.8 eV and 401.0 eV, attributed to the sp^2-hybridized N (C–N=C), tertiary N (N–$(C)_3$) and amino group (C–N–H), respectively. Thus, these observations further indicate the formation of the K-PHI films. These N 1s peaks are also found to weaken in intensity upon etching with Ar^+, showing the instability of the heptazine ring against Ar^+ bombardment.[64]

High-resolution XPS spectra of S 2p and Sn 3d are presented in Fig. 3c and d, respectively. As shown in Fig. 3c, in the S 2p spectrum, two peaks can be observed with binding energies of 162.5 eV and 161.3 eV, attributed to S $2p_{1/2}$ and S $2p_{3/2}$, respectively. Consistently, as shown in Fig. 3d, in the Sn spectrum, two peaks can be observed at 494.8 eV and 486.5 eV, attributed to the Sn $3d_{3/2}$ and $3d_{5/2}$, respectively. As shown in the depth profiles of the S 2p and Sn 3d spectra shown in Fig. 3c and d, both peaks due to S 2p and Sn 3d increase in intensity upon etching with Ar^+, indicating that SnS_2 is abundant even near to the FTO and acts as crystal seeds even at the bottom of the K-PHI films. Moreover, the binding energy of Sn 3d was found to decrease gradually from the top to the bottom of the films, revealing that S is not homogeneously present nor bonded with Sn, especially near to the FTO layer, while it bonds with C belonging to K-PHI.

The band structure of the K-PHI based photoanode was studied by UV-DRS. As shown in Fig. 3e, two characteristic absorption bands are observed at a wavelength region shorter than 470 nm and at around 500 nm. Corresponding to the Kubelka–Munk plots (Fig. S10†), the bandgap energies are defined to be 2.66 eV for K-PHI and 2.75 eV for melon. Thus, the absorption of K-PHI is observed in the visible light region, being much longer in wavelength than that of melon. In addition, a long tail can be seen in the Kubelka–Munk plots of K-PHI (Fig. S10b†), assigned to a sub-bandgap of *ca.* 2.28 eV due to SnS_2 moieties. Digital photographs of melon and K-PHI were acquired (Fig. S11†), with their optical properties being in good agreement with their UV-DRS spectra (Fig. 3e). Furthermore, the conduction band minimum (CBM) and valence band maximum (VBM) of melon and K-PHI were defined not only by experimental but also by theoretical approaches.

The Mott–Schottky data of the electrochemical impedance spectroscopy (EIS) were plotted to determine the flat band potentials of melon and the K-PHI films, which are associated

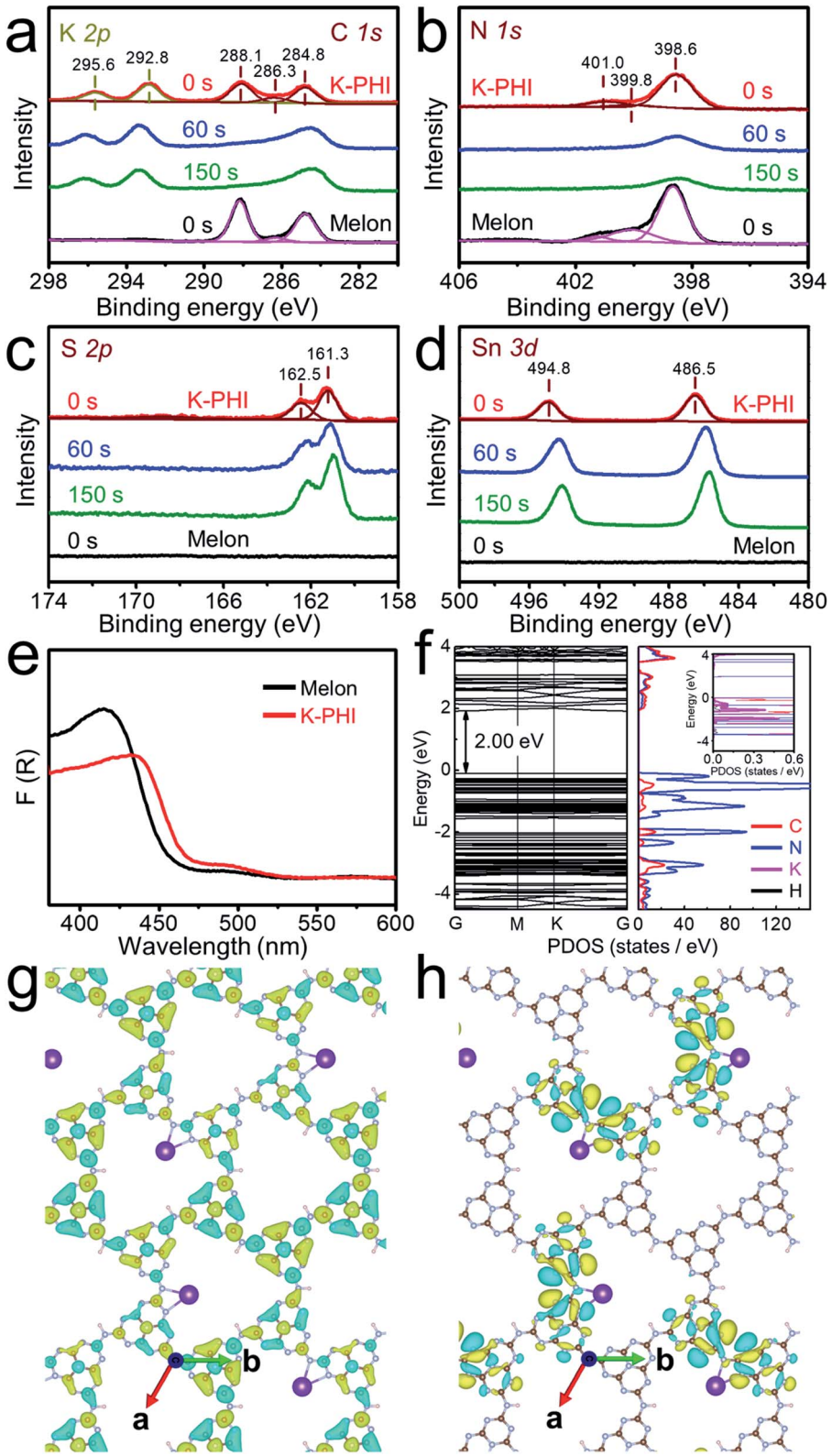

Fig. 3 High-resolution XPS spectra of melon and XPS depth profiles of K-PHI. (a) K 2p and C 1s. (b) N 1s. (c) K 2p. (d) Sn 3d. (e) UV-DRS spectra of melon and K-PHI. (f) Calculated band structure and the corresponding projected density of states (PDOS) for K-PHI. Orbital diagrams of the (g) CBM and (h) VBM of K-PHI. The orbitals with cyan and yellow colors represent the positive and negative values of the molecular orbitals. The pink, brown, gray, and purple balls represent H, C, N, and K atoms, respectively.

with the CBMs of the samples (Fig. S12†). From these results, the band structures of melon (CBM; −0.50 V and VBM; 2.25 V *versus* RHE) and K-PHI (CBM; −0.48 V and VBM; 2.18 V *versus* RHE) were defined (Fig. S13†). In comparison with melon, the potential energy of the CBM of K-PHI was found to shift towards the positive direction by 0.02 V and the VBM shifted towards the negative direction by 0.07 V. Therefore, the bandgap of the K-PHI is smaller than that of melon by 0.05 V, while the CBM and VBM potentials of K-PHI still surpass the redox potentials for water splitting and are thermodynamically sufficient for the evolution of hydrogen and oxygen from water.

DFT was applied to compare the bandgap energies of melon and K-PHI. As shown in Fig. 3f, the VBM of K-PHI is mainly constructed from N and the CBM is constructed from a combination of C and N, similar to that of melon (Fig. S14†). Note that the K makes a relatively weak contribution to the construction of the VBM. As shown in Fig. 3g and h, the VBM of K-PHI is mostly localized in the vicinity of the K^+ cation, while the CBM of K-PHI is delocalized on the heptazine rings, being different from those of PHI (Fig. S15†), in which the VBM and CBM exhibit a significant overlap on the heptazine rings. These theoretically calculated electronic structures clearly suggest that, compared to melon and PHI, the K-PHI exhibits high activity for the water splitting reaction due to the improved charge separation of the photogenerated charge carriers and their migration.

PEC water splitting was studied using a three-electrode configuration employing 1.0 M NaOH as an electrolyte solution under AM 1.5G illumination. Linear sweep voltammetry (LSV) measurements of the K-PHI photoanode are displayed in Fig. 4a. In comparison with the melon photoanode, a remarkably enhanced photocurrent density of 0.80 mA cm^{-2} was achieved with the K-PHI photoanode at a voltage bias of 1.23 V *vs.* RHE in 1.0 M NaOH electrolyte solution under AM 1.5G illumination (Fig. 4). Such enhancement can be attributed to improved charge transfer in highly-crystalline K-PHI. This value is much higher than those of the PCN-based photoanodes reported in the literature (Table S1†), *ca.* 20 times higher than that of the melon-based photoanode.

The ion concentration of the electrolyte solution influences the surface redox reactions in the PEC system. Therefore, the dependences of the photocurrent density were measured as a function of NaOH concentration (Fig. S16†). When the reaction was operated at 0.1 M and 0.5 M NaOH, the photocurrent densities were *ca.* 0.55 mA cm^{-2} and 0.65 mA cm^{-2}, respectively. The photocurrent density reached 0.80 mA cm^{-2} at 1.0 M NaOH, and then remained at this value upon a further increase in concentration. Thus, the concentration of the hydroxyl ion is strongly related to the rate of the oxygen evolution at the photoanode, and 1.0 M of hydroxyl ions was found to be the optimal concentration for oxygen evolution at the K-PHI photoanode.

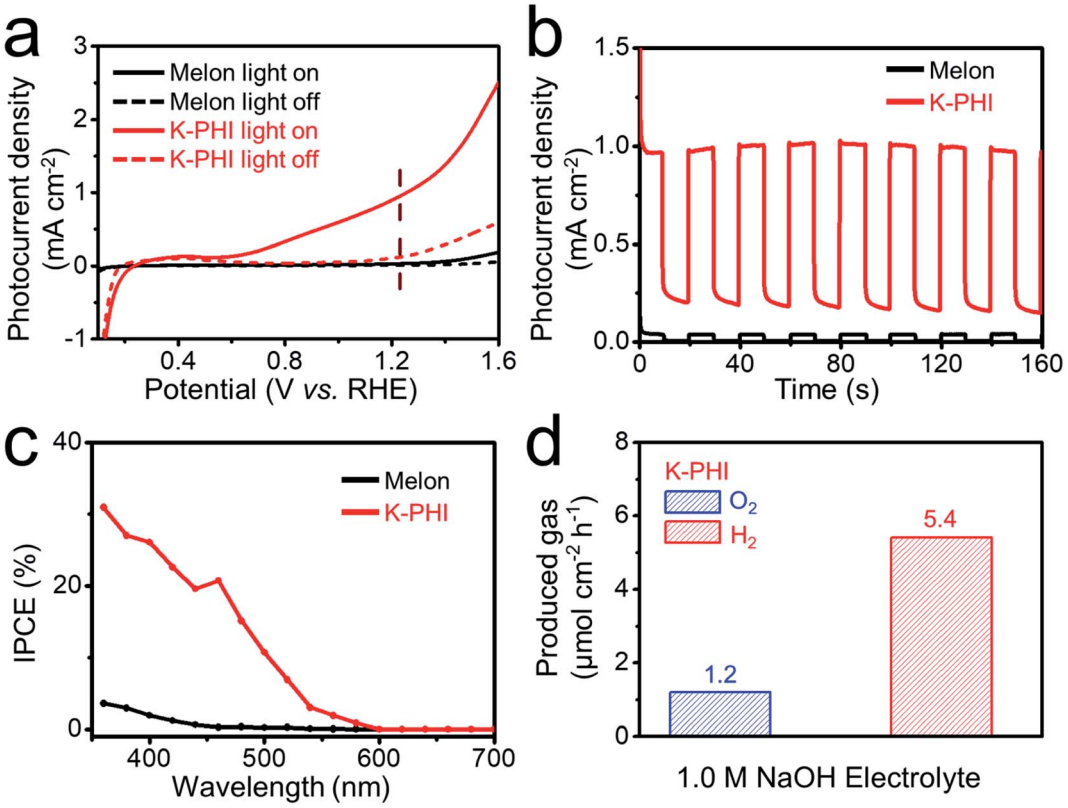

Fig. 4 (a) LSV curves of the melon and K-PHI photoanodes under AM 1.5G illumination (solid curves) and in the absence of illumination (dash curves) in 1.0 M NaOH aqueous solution. (b) Photocurrent densities of the melon and K-PHI photoanodes in 1.0 M NaOH aqueous solution at 1.23 V *vs.* RHE. (c) IPCE plots of the melon and K-PHI photoanodes in 1.0 M NaOH aqueous solution at 1.23 V *vs.* RHE. (d) Evolution rates of oxygen and hydrogen gases by the K-PHI photoanode under an applied voltage of 1.23 V (*vs.* RHE).

The incident photon-to-electron conversion efficiency (IPCE) was investigated. As shown in Fig. 4c, the optimal efficiency was recorded to be *ca.* 30% at an incident wavelength of 360 nm. This photoanode is efficiently enabled to convert incident visible light at 420 nm to an IPCE of *ca.* 22%. Note that a shoulder peak on the IPCE spectrum at a wavelength of *ca.* 460 nm can probably be attributed to the contribution of SnS_2 moieties in the photoanode. To confirm this, a reference experiment was conducted with powder-based photoanode containing 2.65 at% SnS_2 in the K-PHI films (Fig. S17†). In comparison with the pristine K-PHI photoanode, the K-PHI blended with SnS_2 powder exhibited a photocurrent density of only *ca.* 3.5 μA cm^{-2}, much lower than that achieved for the *in situ* synthesized K-PHI photoanode. Thus, these results clearly exhibit that the promotion effect of SnS_2 moieties in the K-PHI photoanode can be excluded and at the same time suggest the importance of efficient charge migration in the highly crystallized polymeric films as a photoelectrode. To confirm the conductivity of the photoanode, a four-point probe was applied to determine the sheet resistance of SnS_2/FTO glass that was prepared by scraping off the K-PHI films (Fig. S18†), giving a value of *ca.* 7 Ω sq^{-1}, a value that is the same as that of the original FTO glass.

The water splitting reaction was conducted using the K-PHI photoanode for an hour (Fig. S19†), during which time the photocurrent density gradually degraded. To understand the reasons for the degradation, different characterization methods, including SEM, PXRD and XPS, were used to study the photoanode after testing. It is obvious that although the K-PHI films are exfoliated by the water splitting reaction, as shown in SEM images (Fig. S20†), the chemical structure of K-PHI is generally preserved (Fig. S21†). Note that the peak intensity of SnS_2 in the PXRD pattern (Fig. S21a†) decreases after the measurement, indicating that the instability of the films are probably related to the SnS_2 seed layer, which is unstable in basic solution. The amounts of evolved oxygen and hydrogen were measured, with the results shown in Fig. 4d. The photocurrent density and the signal intensity of gas chromatographs corresponding to the evolved gases were measured against the reaction time (Fig. S22†). The evolution rates of O_2 and H_2 in 1.0 M NaOH aqueous solution were determined to be 1.2 and 5.4 μmol cm^{-2} h^{-1}, respectively, and the corresponding faradaic efficiencies were measured as *ca.* 30% and 70%, respectively, for the splitting of water. The maximum ABPE was also determined to be *ca.* 0.15% at a bias of 0.90 V (*vs.* RHE) (Fig. S23†).

To investigate the origin of the improved charge transfer in the K-PHI photoanode, steady-state and *operando* approaches were carried out. The PL spectra of melon and K-PHI were measured at room temperature to study the steady-state behavior of the photogenerated charge carriers. As shown in Fig. S24,† the PL spectra were observed at around 450 nm by the excitation of the samples at a wavelength of 360 nm. Furthermore, to gain information on the dynamics of the photogenerated charge carriers, the transient decay curves of the PL of these samples were measured under excitation at a wavelength of 360 nm. As shown in Fig. 5a, the transient decay PL of the K-PHI photoanode is much faster than that of the melon photoanode. The lifetime of the charge carriers in K-PHI was determined to be *ca.* 0.52 ns by the analysis of the decay curve, being significantly shorter than that of the melon photoanode, which has a value of *ca.* 2.83 ns. The results reveal that K-PHI shows significant enhancement in its photoexcitation charge migration. The accelerated migration compensates for the weakness of amorphous melon to improve the performance for water splitting.

Charge carrier density was estimated from Mott–Schottky plots of the EIS data according to the Mott–Schottky relationship. As shown in Fig. 5b, the carrier density of the K-PHI photoanode is *ca.* 10^{22} cm^{-3}, three orders of magnitude greater than that of the melon photoanode. Nyquist plots of the EIS data of melon and K-PHI were conducted to measure the charge transfer resistance, trapping of holes in the surface states, steady state concentration of the trapped holes, and more, under the same conditions as those used in water splitting. The equivalent circuits and impedance spectra are presented and analyzed in Fig. S25.† The charge transfer resistance (R_{ct}) was measured without light illumination. The R_{ct} of the K-PHI photoanode was found to be *ca.* 10 times lower than that of the melon photoanode, indicating that the intrinsic resistance decreases in the highly crystalline K-PHI films. Under the conditions of AM 1.5G illumination, both charge transfer resistance from the surface to solution ($R_{ct,ss}$) and the resistance of trapped holes in the surface state (R_{trap}) for K-PHI were found to be lower than those of melon by one order of magnitude. These results clearly indicate that the transfer rate of the photogenerated holes is significantly promoted in K-PHI. Furthermore, the steady state concentration of trapped holes (C_{ss}) in the K-PHI photoanode was found to be higher than that of the amorphous melon photoanode. These results clearly indicate that K-PHI has the capacity to trap a greater number of holes than melon, with these holes attributed to the oxidation reaction. Thus, all of the results suggest that the K-PHI photoanode not only produces more holes efficiently, but also improves their transfer to induce the oxidation reaction efficiently.

IMPS was applied to investigate the kinetics of the photoanodes under water-splitting conditions. Random signals were observed in the IMPS response of the melon photoanode (Fig. S26†), therefore meaning that kinetics information could not be identified for melon. Such non-quantifiable behavior is attributed to the amorphous structure of the melon films that has a degree of polymerization. While, as shown in Fig. 5c, the K-PHI photoanode exhibits two characteristic semicircles in its IMPS spectra. The kinetics of the photogenerated charge carriers are exemplified by the first-order rate constants of charge transfer (K_t) and surface recombination (K_r), and the values for melon and K-PHI are shown in Fig. 5d. As expected and observed in Fig. 5d, an increment in bias potential leads to an increase in the rate constant of the charge transfer, since a sufficient bias potential increases band bending, leading to efficient separation of the photogenerated charge carriers into free electrons and holes, and also the suppression of the rate of recombination of electrons and holes. As can be seen from Fig. 5d, the critical voltage of the bias potential for the K-PHI is *ca.* 0.78 V (*vs.* RHE). When the bias potential applied is greater than this value, the rate constant of the charge transfer (K_t)

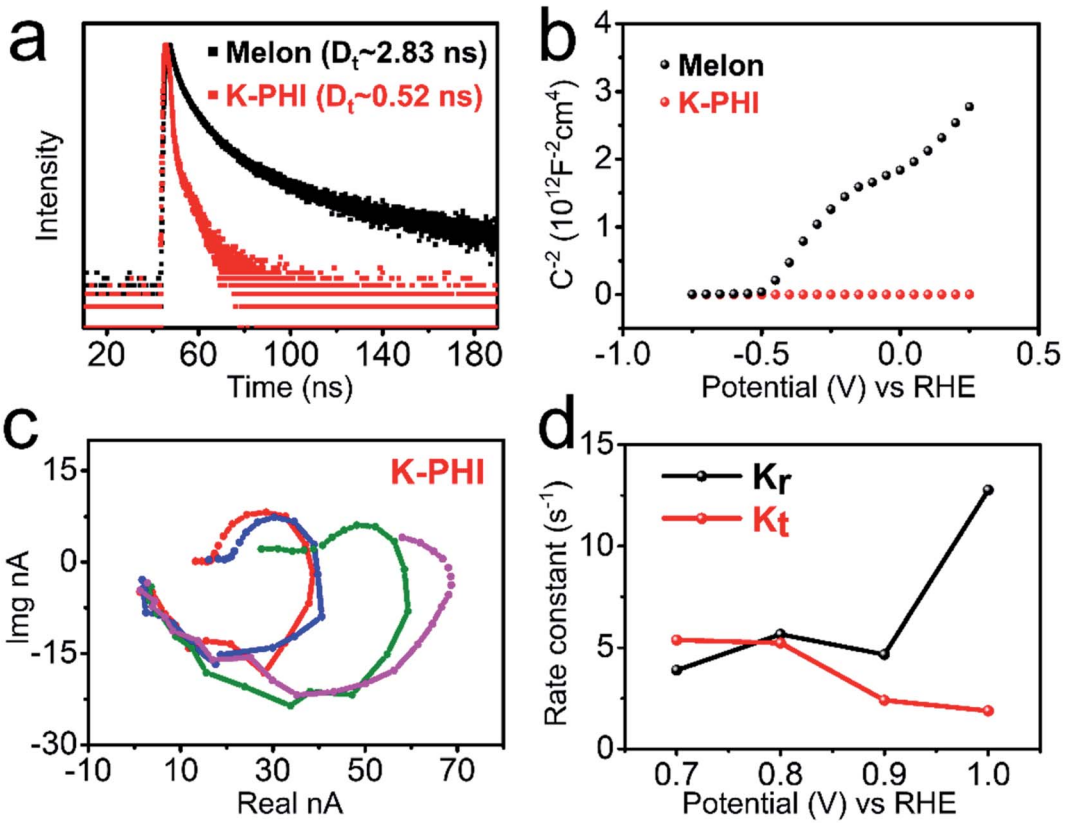

Fig. 5 (a) The transient decay of the PL of melon and K-PHI. (b) Mott–Schottky plots of the EIS measurements of the melon and K-PHI photoanodes. (c) IMPS of the K-PHI photoanode. (d) Potential dependence of the rate constants K_t and K_r as a function of applied potential for the K-PHI photoanode.

becomes dominant under light illumination, and thus, it is kinetically favorable for the electrons and holes to induce the water splitting reaction. These results further indicate the importance of the high crystallinity of PCN materials for their application in the water splitting reaction.

Conclusions

A highly-crystalline K-PHI photoanode was fabricated *via in situ* polymerization. The highly-crystalline CN polymer photoanode was successfully applied to drive PEC water splitting to evolve hydrogen and oxygen, and a remarkable high photocurrent density, *ca.* 0.80 mA cm^{-2}, was realized under the conditions of AM 1.5G illumination in 1.0 M NaOH electrolyte solution without any sacrificial agents. From results obtained using a melon-based photoanode, it can be deduced that the high performance of K-PHI can be mainly attributed to the improved crystallinity of the material, which leads to significant improvement in the transfer of charge carriers. The kinetics of the charge carriers were investigated by applying steady state and *operando* approaches, which also clearly exhibited the importance of the crystallinity of PCN for efficient charge carrier transfer in polymer photoelectrodes. The present results provide an opportunity and clues as to how to approach the practical utilization of a PEC system for the production of hydrogen from water and other advanced applications.[65,66]

Data availability

We have presented all the data that relating to this work in this manuscript and ESI.†

Author contributions

Xiaochun Li: investigation, methodology, formal analysis, data curation, visualization, writing – original draft. Xiaoxiao Chen: formal analysis, data curation, visualization, writing – review and editing. Yuanxing Fang: conceptualization, methodology, formal analysis, investigation, resources, writing – review and editing, visualization, supervision, project administration, funding acquisition. Wei Lin: writing – review and editing. Yidong Hou: writing – review and editing. Masakazu Anpo: writing – review and editing. Xianzhi Fu: writing – review and editing. Xinchen Wang: conceptualization, writing – review and editing, supervision, project administration, funding acquisition.

Conflicts of interest

There are no conflicts to declare.

Acknowledgements

This work was supported by the National Natural Science Foundation of China (21961142019, 22075047, U1905214, 21761132002 and 21861130353), the National Key R&D Program of China (2018YFA0209301), the 111 Project (D16008), and the Chang Jiang Scholars Program of China (T2016147).

Notes and references

1 C. Jiang, S. J. A. Moniz, A. Wang, T. Zhang and J. Tang, *Chem. Soc. Rev.*, 2017, **46**, 4645–4660.
2 Z. Wang, C. Li and K. Domen, *Chem. Soc. Rev.*, 2019, **48**, 2109–2125.
3 C. Feng, F. Wang, Z. Liu, M. Nakabayashi, Y. Xiao, Q. Zeng, J. Fu, Q. Wu, C. Cui, Y. Han, N. Shibata, K. Domen, I. D. Sharp and Y. Li, *Nat. Commun.*, 2021, **12**, 5980.
4 H. Nishiyama, T. Yamada, M. Nakabayashi, Y. Maehara, M. Yamaguchi, Y. Kuromiya, Y. Nagatsuma, H. Tokudome, S. Akiyama, T. Watanabe, R. Narushima, S. Okunaka, N. Shibata, T. Takata, T. Hisatomi and K. Domen, *Nature*, 2021, **598**, 304–307.
5 X. Li, J. Wang, Y. Fang, H. Zhang, X. Fu and X. Wang, *Acc. Mater. Res.*, 2021, **2**, 933–943.
6 S. Cao, Y. Wu, J. Hou, B. Zhang, Z. Li, X. Nie and L. Sun, *Adv. Energy Mater.*, 2020, **10**, 1902935.
7 T. An, J. Tang, Y. Zhang, Y. Quan, X. Gong, A. M. Al-Enizi, A. A. Elzatahry, L. Zhang and G. Zheng, *ACS Appl. Mater. Interfaces*, 2016, **8**, 12772–12779.
8 S. Xue, W. Huang, W. Lin, W. Xing, M. Shen, X. Ye, X. Liang, C. Yang, Y. Hou, Z. Yu and X. Wang, *Chem Catal.*, 2022, **2**, 125–139.
9 X. Ye, C. Wei, S. Xue, W. Xing, X. Liang, H. Nie, M. Shen, Y. Du, J. Zhang, X. Wang, W. Lin and Z. Yu, *ACS Appl. Mater. Interfaces*, 2022, **14**, 2194–2201.
10 T. Oshima, T. Ichibha, K. S. Qin, K. Muraoka, J. J. M. Vequizo, K. Hibino, R. Kuriki, S. Yamashita, K. Hongo, T. Uchiyama, K. Fujii, D. Lu, R. Maezono, A. Yamakata, H. Kato, K. Kimoto, M. Yashima, Y. Uchimoto, M. Kakihana, O. Ishitani, H. Kageyama and K. Maeda, *Angew. Chem., Int. Ed.*, 2018, **57**, 8154–8158.
11 L. Ran, S. Qiu, P. Zhai, Z. Li, J. Gao, X. Zhang, B. Zhang, C. Wang, L. Sun and J. Hou, *J. Am. Chem. Soc.*, 2021, **143**, 7402–7413.
12 K. Ogawa, H. Suzuki, C. Zhong, R. Sakamoto, O. Tomita, A. Saeki, H. Kageyama and R. Abe, *J. Am. Chem. Soc.*, 2021, **143**, 8446–8453.
13 M. Volokh, G. Peng, J. Barrio and M. Shalom, *Angew. Chem., Int. Ed.*, 2019, **58**, 6138–6151.
14 Y. Fang, Y. Ma, M. Zheng, P. Yang, A. M. Asiri and X. Wang, *Coord. Chem. Rev.*, 2018, **373**, 83–115.
15 M. Xu, D. Li, K. Sun, L. Jiao, C. Xie, C. Ding and H.-L. Jiang, *Angew. Chem., Int. Ed.*, 2021, **60**, 16372–16376.
16 Y. Ma, J. Du, Y. Fang and X. Wang, *ChemSusChem*, 2021, **14**, 946–951.
17 R. Kuriki, M. Yamamoto, K. Higuchi, Y. Yamamoto, M. Akatsuka, D. Lu, S. Yagi, T. Yoshida, O. Ishitani and K. Maeda, *Angew. Chem., Int. Ed.*, 2017, **56**, 4867–4871.
18 Y. Fang and X. Wang, *Angew. Chem., Int. Ed.*, 2017, **56**, 15506–15518.
19 B. Dong, J. Cui, Y. Gao, Y. Qi, F. Zhang and C. Li, *Adv. Mater.*, 2019, **31**, 1808185.
20 L. Yang, H. Chen, Y. Xu, R. Qian, Q. Chen and Y. Fang, *Chem. Eng. Sci.*, 2022, **251**, 117435.
21 Z. Luo, X. Ye, S. Zhang, S. Xue, C. Yang, Y. Hou, W. Xing, R. Yu, J. Sun, Z. Yu and X. Wang, *Nat. Commun.*, 2022, **13**, 2230.
22 W.-J. Ong, L.-L. Tan, Y. H. Ng, S.-T. Yong and S.-P. Chai, *Chem. Rev.*, 2016, **116**, 7159–7329.
23 X. Wang, K. Maeda, A. Thomas, K. Takanabe, G. Xin, J. M. Carlsson, K. Domen and M. Antonietti, *Nat. Mater.*, 2009, **8**, 76–80.
24 G. Zhang, M. Zhang, X. Ye, X. Qiu, S. Lin and X. Wang, *Adv. Mater.*, 2014, **26**, 805–809.
25 Y. Fang, X. Li, Y. Wang, C. Giordano and X. Wang, *Appl. Catal., B*, 2020, **268**, 118398.
26 Y. Yang, S. Wang, Y. Jiao, Z. Wang, M. Xiao, A. Du, Y. Li, J. Wang and L. Wang, *Adv. Funct. Mater.*, 2018, **28**, 1805698.
27 Y. Chen, J. Zhang, M. Zhang and X. Wang, *Chem. Sci.*, 2013, **4**, 3244–3248.
28 Y. Fang, Y. Hou, X. Fu and X. Wang, *Chem. Rev.*, 2022, **122**, 4204–4256.
29 L. Lin, H. Ou, Y. Zhang and X. Wang, *ACS Catal.*, 2016, **6**, 3921–3931.
30 I. Osaka and K. Takimiya, *Polymer*, 2015, **59**, A1–A15.
31 Y. Ma, Y. Liu, T. Yu, W. Lai, Z. Ge and Z. Jiang, *RSC Adv.*, 2019, **9**, 3120–3127.
32 L. Lin, C. Wang, W. Ren, H. Ou, Y. Zhang and X. Wang, *Chem. Sci.*, 2017, **8**, 5506–5511.
33 L. Lin, Z. Lin, J. Zhang, X. Cai, W. Lin, Z. Yu and X. Wang, *Nat. Catal.*, 2020, **3**, 649–655.
34 A. Savateev, N. V. Tarakina, V. Strauss, T. Hussain, K. ten Brummelhuis, J. M. Sánchez Vadillo, Y. Markushyna, S. Mazzanti, A. P. Tyutyunnik, R. Walczak, M. Oschatz, D. M. Guldi, A. Karton and M. Antonietti, *Angew. Chem., Int. Ed.*, 2020, **59**, 15061–15068.
35 M.-Y. Ye, S. Li, X. Zhao, N. V. Tarakina, C. Teutloff, W. Y. Chow, R. Bittl and A. Thomas, *Adv. Mater.*, 2020, **32**, 1903942.
36 G. Zhang, L. Lin, G. Li, Y. Zhang, A. Savateev, S. Zafeiratos, X. Wang and M. Antonietti, *Angew. Chem., Int. Ed.*, 2018, **57**, 9372–9376.
37 M. Liu, C. Wei, H. Zhuzhang, J. Zhou, Z. Pan, W. Lin, Z. Yu, G. Zhang and X. Wang, *Angew. Chem., Int. Ed.*, 2022, **61**, e202113389.
38 Y. Fang, Y. Xu, X. Li, Y. Ma and X. Wang, *Angew. Chem., Int. Ed.*, 2018, **57**, 9749–9753.
39 J. Albero, E. M. Barea, J. Xu, I. Mora-Seró, H. Garcia and M. Shalom, *Adv. Mater. Interfaces*, 2017, **4**, 1600265.
40 X. Li, J. Wang, J. Xia, Y. Fang, Y. Hou, X. Fu, M. Shalom and X. Wang, *ChemSusChem*, 2022, **15**, e20220330.

41 W. Zhang, J. Albero, L. Xi, K. M. Lange, H. Garcia, X. Wang and M. Shalom, *ACS Appl. Mater. Interfaces*, 2017, **9**, 32667–32677.
42 T. Zhao, Q. Zhou, Y. Lv, D. Han, K. Wu, L. Zhao, Y. Shen, S. Liu and Y. Zhang, *Angew. Chem., Int. Ed.*, 2020, **59**, 1139–1143.
43 G. Peng, M. Volokh, J. Tzadikov, J. Sun and M. Shalom, *Adv. Energy Mater.*, 2018, **8**, 1800566.
44 Y. Fang, X. Li and X. Wang, *ACS Catal.*, 2018, **8**, 8774–8780.
45 J. Xu, S. Cao, T. Brenner, X. Yang, J. Yu, M. Antonietti and M. Shalom, *Adv. Funct. Mater.*, 2015, **25**, 6265–6271.
46 G. Peng, J. Albero, H. Garcia and M. Shalom, *Angew. Chem., Int. Ed.*, 2018, **57**, 15807–15811.
47 J. Xu, H. Wang, C. Zhang, X. Yang, S. Cao, J. Yu and M. Shalom, *Angew. Chem., Int. Ed.*, 2017, **56**, 8426–8430.
48 J. Qin, J. Barrio, G. Peng, J. Tzadikov, L. Abisdris, M. Volokh and M. Shalom, *Nat. Commun.*, 2020, **11**, 4701.
49 P. Yang, H. Ou, Y. Fang and X. Wang, *Angew. Chem., Int. Ed.*, 2017, **56**, 3992–3996.
50 J. Resasco, H. Zhang, N. Kornienko, N. Becknell, H. Lee, J. Guo, A. L. Briseno and P. Yang, *ACS Cent. Sci.*, 2016, **2**, 80–88.
51 X. Li, Z. Cheng, Y. Fang, X. Fu and X. Wang, *Sol. RRL*, 2020, **4**, 2000168.
52 Y. Xiao, C. Feng, J. Fu, F. Wang, C. Li, V. F. Kunzelmann, C.-M. Jiang, M. Nakabayashi, N. Shibata, I. D. Sharp, K. Domen and Y. Li, *Nat. Catal.*, 2020, **3**, 932–940.
53 G. Kresse and J. Furthmüller, *Phys. Rev. B: Condens. Matter Mater. Phys.*, 1996, **54**, 11169–11186.
54 G. Kresse and J. Furthmüller, *Comput. Mater. Sci.*, 1996, **6**, 15–50.
55 P. E. Blöchl, *Phys. Rev. B: Condens. Matter Mater. Phys.*, 1994, **50**, 17953–17979.
56 G. Kresse and D. Joubert, *Phys. Rev. B: Condens. Matter Mater. Phys.*, 1999, **59**, 1758–1775.
57 J. P. Perdew, K. Burke and M. Ernzerhof, *Phys. Rev. Lett.*, 1996, **77**, 3865–3868.
58 S. Grimme, *J. Comput. Chem.*, 2006, **27**, 1787–1799.
59 H. J. Monkhorst and J. D. Pack, *Phys. Rev. B: Solid State*, 1976, **13**, 5188–5192.
60 J. Mu, H. Miao, E. Liu, L. Chen, J. Feng, T. Han, Y. Gao, J. Fan and X. Hu, *Ceram. Int.*, 2017, **43**, 4992–5001.
61 J. Zhang, M. Zhang, G. Zhang and X. Wang, *ACS Catal.*, 2012, **2**, 940–948.
62 L. Lin, W. Ren, C. Wang, A. M. Asiri, J. Zhang and X. Wang, *Appl. Catal., B*, 2018, **231**, 234–241.
63 H. Gao, S. Yan, J. Wang, Y. A. Huang, P. Wang, Z. Li and Z. Zou, *Phys. Chem. Chem. Phys.*, 2013, **15**, 18077–18084.
64 H. Yu, R. Shi, Y. Zhao, T. Bian, Y. Zhao, C. Zhou, G. I. N. Waterhouse, L.-Z. Wu, C.-H. Tung and T. Zhang, *Adv. Mater.*, 2017, **29**, 1605148.
65 D. Kong, Y. Zheng, M. Kobielusz, Y. Wang, Z. Bai, W. Macyk, X. Wang and J. Tang, *Mater. Today*, 2018, **21**, 897–924.
66 C. Feng, Z. Wang, Y. Ma, Y. Zhang, L. Wang and Y. Bi, *Appl. Catal., B*, 2017, **205**, 19–23.